OPEN ACCESS



Atmospheric Characterization of the Super-Jupiter HIP 99770 b with KPIC

Yapeng Zhang^{1,14}, Jerry W. Xuan¹, Dimitri Mawet¹, Jason J. Wang², Chih-Chun Hsu², Jean-Bapiste Ruffio³, Heather A. Knutson⁴, Julie Inglis⁴, Geoffrey A. Blake⁴, Yayaati Chachan^{5,6,15}, Katelyn Horstman¹, Ashley Baker¹, Randall Bartos⁷, Benjamin Calvin⁸, Sylvain Cetre⁹, Jacques-Robert Delorme⁹, Greg Doppmann⁹, Daniel Echeverri¹, Luke Finnerty⁸, Michael P. Fitzgerald⁸, Nemanja Jovanovic¹, Joshua Liberman^{1,10}, Ronald A. López⁸, Evan Morris¹¹, Jacklyn Pezzato¹, Ben Sappey³, Tobias Schofield¹, Andrew Skemer¹¹, J. Kent Wallace⁷, Ji Wang¹², and Clarissa R. Do Ó¹³ ¹ Department of Astronomy, California Institute of Technology, Pasadena, CA 91125, USA ² Center for Interdisciplinary Exploration and Research in Astrophysics (CIERA) and Department of Physics and Astronomy, Northwestern University, Evanston, IL 60208, USA ³ Department of Astronomy & Astrophysics, University of California, San Diego, La Jolla, CA 92093, USA Division of Geological & Planetary Sciences, California Institute of Technology, Pasadena, CA 91125, USA ⁵ Department of Physics and Trottier Space Institute, McGill University, 3600 rue University, Montreal, QC H3A 2T8, Canada Trottier Institute for Research on Exoplanets (iREx), Université de Montréal, Canada ⁷ Jet Propulsion Laboratory, California Institute of Technology, 4800 Oak Grove Dr., Pasadena, CA 91109, USA ⁸ Department of Physics & Astronomy, 430 Portola Plaza, University of California, Los Angeles, CA 90095, USA W. M. Keck Observatory, 65-1120 Mamalahoa Hwy., Kamuela, HI, USA James C. Wyant College of Optical Sciences, University of Arizona, Meinel Building 1630 E. University Blvd., Tucson, AZ 85721, USA Department of Astronomy & Astrophysics, University of California, Santa Cruz, Santa Cruz, CA95064, USA Department of Astronomy, The Ohio State University, 100 W. 18th Ave., Columbus, OH 43210 USA Department of Physics, University of California, San Diego, La Jolla, CA 92093, USA Received 2024 May 13; revised 2024 June 21; accepted 2024 July 19; published 2024 August 27

Abstract

Young, self-luminous super-Jovian companions discovered by direct imaging provide a challenging test for planet formation and evolution theories. By spectroscopically characterizing the atmospheric compositions of these super-Jupiters, we can constrain their formation histories. Here we present studies of the recently discovered HIP 99770 b, a 16 $M_{\rm Jup}$ high-contrast companion on a 17 au orbit, using the fiber-fed high-resolution spectrograph KPIC ($\mathcal{R} \sim 35,000$) on the Keck II telescope. Our K-band observations led to detections of H₂O and CO in the atmosphere of HIP 99770 b. We carried out free retrieval analyses using petitral parameters to measure its chemical abundances, including the metallicity and C/O ratio, projected rotation velocity ($v \sin i$), and radial velocity (RV). We found that the companion's atmosphere has $C/O = 0.55^{+0.06}_{-0.04}$ and [M/H] = $0.26^{+0.24}_{-0.23}$ (1σ confidence intervals), values consistent with those of the Sun and with a companion formation via gravitational instability or core accretion. The projected rotation velocity $v \sin(i) < 7.8 \, \mathrm{km \, s^{-1}}$ is small relative to other directly imaged companions with similar masses and ages. This may imply a nearly pole-on orientation or effective magnetic braking by a circumplanetary disk. In addition, we added the companion-to-primary relative RV measurement to the orbital fitting and obtained updated constraints on orbital parameters. Detailed characterization of super-Jovian companions within 20 au like HIP 99770 b is critical for understanding the formation histories of this population.

Unified Astronomy Thesaurus concepts: Exoplanet atmospheres (487); High resolution spectroscopy (2096); Substellar companion stars (1648)

1. Introduction

Young, self-luminous super-Jovian companions discovered by direct imaging surveys have posed significant challenges to planet formation theories. These objects typically straddle the mass boundary between planets and brown dwarfs (\sim 13 $M_{\rm Jup}$) and orbit their primary stars at large separations (>10 au). Their formation mechanisms remain under debate, as they are not easily compatible with either in situ core accretion or gravitational instability (Pollack et al. 1996; Boss 1997;

Original content from this work may be used under the terms of the Creative Commons Attribution 4.0 licence. Any further distribution of this work must maintain attribution to the author(s) and the title of the work, journal citation and DOI.

Chabrier 2003; Kratter & Lodato 2016). The long timescale of core accretion in the outer protoplanetary disk makes it challenging to assemble massive cores to trigger runaway accretion before the gas disk dissipates (Lambrechts & Johansen 2012), while disk instability and cloud fragmentation are expected to form more massive objects like brown dwarfs or stellar companions (Zhu et al. 2012; Forgan & Rice 2013; Offner et al. 2023). For some wide-orbit companions at hundreds of au, formation at closer orbits followed by scattering events may be effective (Veras et al. 2009). Previous studies on orbital architectures of these super-Jupiters (<20 $M_{\rm Jup}$) versus those of brown dwarfs (>20 $M_{\rm Jup}$) found evidence for distinct distributions in their semimajor axes and orbital eccentricities (Nielsen et al. 2019; Bowler et al. 2020; Do Ó et al. 2023; Nagpal et al. 2023). This suggests that the two populations likely have distinct formation mechanisms, but it is unclear whether there is a well-defined boundary separating them.

¹⁴ 51 Pegasi b fellow.

¹⁵ CITA National Fellow.

Atmospheric characterization provides an important avenue to distinguish between competing formation mechanisms for substellar companions. Elemental abundances including the metallicity [M/H] and carbon-to-oxygen (C/O) ratios have been suggested as probes for planet formation (e.g., Öberg et al. 2011; Madhusudhan 2012; Turrini et al. 2021). In general, formation via gravitational instability or cloud fragmentation is thought to result in compositions akin to stars, while core accretion can result in a variety of compositions depending on the accretion mechanisms, formation location relative to disk ice lines, and migration histories (e.g., Madhusudhan et al. 2014; Mordasini et al. 2016; Bitsch et al. 2019), among other factors. Although companions formed via gravitational collapse can also be enriched through late accretion, the impact on their compositions is not expected to be significant because of the high envelope masses (Inglis et al. 2024).

Super-Jupiters on wide orbits are excellent targets for directly probing planetary emission at high signal-to-noise ratio (S/N), therefore allowing for robust constraints on their chemical compositions. As measurements of atmospheric C/O and metallicity in directly imaged super-Jupiters have accumulated over the past few years, we have begun to build a sample large enough to test the hypotheses. Spectral surveys of substellar companions with masses of 10-30 $M_{\rm Jup}$, such as Hoch et al. (2023) and Xuan et al. (2024a), suggest that they display broadly solar compositions, which are chemically compatible with formation via gravitational instability or core accretion beyond CO ice lines, where solids have approximately stellar C/O ratios. Although the planetesimal accretion scenario is less likely for wide-orbit massive gas giants, pebble accretion, whose efficiency increases in the outer disk, is not precluded (Lambrechts & Johansen 2012; Bitsch et al. 2015, 2019).

At an individual system level, linking the atmospheric composition of a planet to its formation history is complicated by a chain of processes, including dust and ice/vapor chemistry evolution in disks, planet migration, late solid enrichment, and mixing of a planet's core and envelope (Mollière et al. 2022). These convoluted processes make inferring a planet's formation history from its current atmosphere difficult. The challenging nature of this task calls for combining different lines of evidence from atmospheric tracers such as refractoryto-volatile ratios (Lothringer et al. 2021; Chachan et al. 2023) and isotopologue ratios (Zhang et al. 2021b, 2021a), as well as dynamical indicators such as spin and orbital architecture (Bryan et al. 2018, 2020a; Xuan et al. 2020). High-resolution spectroscopy of super-Jovian companions provides information on these various aspects simultaneously, enabling a more comprehensive understanding of the current state of the planetary system and its potential connection to formation pathways and evolutionary history.

Despite extensive studies of wide-orbit companions (e.g., Zhang et al. 2021a; Palma-Bifani et al. 2023; Xuan et al. 2024a; Inglis et al. 2024; Petrus et al. 2024), there are relatively few published spectral characterizations of companions with orbital separation within 20 au, which represents a critical region of the parameter space for understanding population-level trends. Most super-Jovian companions with compositional measurements are located beyond 50 au, with only a handful of exceptions, such as β Pic b (GRAVITY Collaboration et al. 2020; Landman et al. 2024), HR 8799 cde (Konopacky et al. 2013; Mollière et al. 2020; Ruffio et al. 2021; Wang et al. 2022;

Nasedkin et al. 2024), 51 Eri b (Brown-Sevilla et al. 2023; Whiteford et al. 2023), and AF Lep b (Zhang et al. 2023; Palma-Bifani et al. 2024). Planets with cooler temperatures and/or smaller separations are more challenging to characterize because of the predominant stellar speckle contamination. Techniques that combine both the spatial and spectral resolving capability have proven to be powerful for enhancing the contrast limit of detection and characterization (Snellen et al. 2015; Hoeijmakers et al. 2018; Agrawal et al. 2023; Ruffio et al. 2023). New instruments coupling adaptive optics systems with high-resolution spectrographs, such as the Keck Planet Imager and Characterizer (KPIC, Mawet et al. 2017), HiRISE on the Very Large Telescope (VLT; Vigan et al. 2024), and REACH on Subaru (Kotani et al. 2020), have recently enabled highresolution spectroscopy of faint companions on close-in orbits (e.g., HR 8799 planets; Wang et al. 2021).

The recently discovered 16 M_{Jup} HIP 99770 b is among only a handful of super-Jovian companions with an orbital separation within 20 au (Currie et al. 2023). Its current location is expected to be within the CO ice line of the protoplanetary disk around A-type host stars (Qi et al. 2015). In core accretion scenarios, the C/O ratio likely varies as a function of the companion's metallicity because of the partitioning of solid versus gas compositions. Therefore, companions at smaller separations are likely to display a larger variety of atmospheric compositions, providing intriguing case studies for testing formation models by measuring both the C/O and metallicity. In contrast, beyond the CO ice line, the companion's C/O ratio is expected to be solar for a wide range of metallicity because most volatiles are condensed out. We note, however, that if the companion has a solar metallicity, it is difficult to distinguish between core accretion and gravitational instability, as both mechanisms can plausibly lead to this outcome, regardless of the planet's birth location.

In this paper, we present the atmospheric characterization of HIP 99770 b using KPIC observations. When combined with its spin velocity and orbital properties, this allows us to place constraints on its formation and evolution. The paper is organized as follows. In Section 2, we introduce the target system HIP 99770. The KPIC observations and data reduction are explained in Section 3. Then, we carry out free retrieval analyses with the observations. The forward model and retrieval framework are described in Section 4. We present the molecular detections and retrieval results in Section 5. We discuss the measured chemical abundances, spin velocity, and their implications for planet formation in Section 6. Finally, we summarize the findings in Section 7.

2. HIP 99770 System

HIP 99770 b is a recently discovered super-Jovian companion with a joint direct imaging and precision astrometry detection (Currie et al. 2023). We summarize the properties of the HIP 99770 system in Table 1. The $1.8\,M_\odot$ A-type primary star HIP 99770 has an effective temperature of $\sim 8000\,\mathrm{K}$, an age of 40–400 Myr, and a distance of 40.74 pc (Gaia Collaboration et al. 2021; Currie et al. 2023). The primary star shows evidence of Hipparcos–Gaia astrometric acceleration induced by an orbiting companion, which was confirmed by direct imaging with the Subaru Coronagraphic Extreme Adaptive Optics Project (SCExAO/CHARIS) and Keck/NIRC2 at an angular separation of 0.44 (Brandt 2021; Currie et al. 2023). The combination of the relative astrometry and

Table 1Properties of the HIP 99770 System

Property	Value	References	
HIP 99770			
$\alpha_{2000.0}$	20:14:32.032	(1)	
$\delta_{2000.0}$	+36:48:22.7	(1)	
Distance (pc)	40.74 ± 0.15	(1)	
$v_{\rm sys}~({\rm km~s}^{-1})$	-20.52 ± 0.40	(1)	
$v \sin i \text{ (km s}^{-1})$	81.1 ± 1.5	(1)	
Age (Myr)	40 (Argus membership)	(2)	
	115-414 (astroseismology)	(2)	
Mass (M_{\odot})	1.85 ± 0.19	(2)	
SpT	A5-A6	(3)	
$T_{\rm eff}$ (K)	8000	(3)	
K_s (mag)	4.42 ± 0.02	(2)	
L_p (mag)	4.40 ± 0.05	(2)	
[C/H]	0.18 ± 0.09	(4)	
[O/H]	0.01 ± 0.09	(4)	
НІР 99770 ь			
SpT	L7-L9.5	(2)	
$T_{\rm eff}$ (K)	1400^{+200}_{-150}	(2)	
K_s (mag)	15.66 ± 0.09	(2)	
L_p (mag)	14.52 ± 0.12	(2)	
a (au)	$16.9^{+3.4}_{-1.9}$	(2)	
Eccentricity	$0.25^{+0.14}_{-0.16}$	(2)	
Mass (M_{Jup})	$16.1^{+5.4}_{-5.0}$	(2)	
Radius (R_{Jup})	1.0 - 1.1	(2)	
$\log g$ (cgs)	4.0 - 4.5	(2)	
$v \sin i \text{ (km s}^{-1})$	$3.5^{+1.7}_{-1.9}$	(5)	
[M/H]	$0.26_{-0.23}^{+0.24}$	(5)	
C/O	$0.55^{+0.06}_{-0.04}$	(5)	

References. (1) Gaia Collaboration et al. 2021; (2) Currie et al. 2023; (3) Murphy & Paunzen 2017; (4) Erspamer & North 2003; Hinkel et al. 2014; (5) this work.

acceleration leads to a dynamical mass of $16.1^{+5.4}_{-5.0}~M_{\rm Jup}$ for the companion, or a companion-to-star mass ratio of $\sim 8 \times 10^{-3}$, at a semimajor axis of $16.9^{+3.4}_{-1.9}$ au and an orbital eccentricity of $0.25^{+0.14}_{-0.16}$ (Currie et al. 2023). The companion's luminosity and dynamical mass are consistent with an age of $115-200~{\rm Myr}$.

Currie et al. (2023) carried out spectral characterization of HIP 99770 b using a CHARIS *JHK* broadband spectrum at 1.16–2.37 μ m and Keck/NIRC2 *L*-band photometry, which suggested a spectral type of L7–L9.5 near the L/T transition, an effective temperature of $T_{\rm eff} \sim 1300-1600$ K, and a surface gravity of log g=4–4.5. Evolutionary models (Baraffe et al. 2003; Spiegel & Burrows 2012) predict a radius of 1.1–1.2 $R_{\rm Jup}$, while the spectral analysis tends to imply a smaller radius of up to 1.05 $R_{\rm Jup}$ (Currie et al. 2023). A comparison to HR 8799 d's spectral shape shows that HIP 99770 b's spectrum is less flat, indicating moderate cloudiness.

3. Observations and Data Reduction

We observed the system with KPIC (Mawet et al. 2017; Delorme et al. 2021; Echeverri et al. 2022) on UT 2023 June 16 and 21. KPIC uses a fiber injection unit located downstream of the Keck II adaptive optics system to inject light into single-mode fibers, which are connected to the NIRSPEC high-resolution ($\mathcal{R} \sim 35,000$) spectrograph (McLean et al. 1998; Martin et al. 2018) to disperse light onto the detector. Among

Table 2KPIC Observations of HIP 99770 b

Date	t _{int} (minutes)	Air Mass	Throughput	S/N
2023-06-16	90	1.1	3.4%	1.0
2023-06-21	60	1.1	3.3%	0.8

Note. The S/N per wavelength channel for the companion is estimated from the residuals (see Figure 1) that include both the background thermal noise and the photon noise due to stellar speckles.

the four illuminated fibers, one of them is aligned to the position of the companion to obtain its spectra. The use of single-mode fibers aids in the suppression of the stellar speckle and sky background and ensures a stable Gaussian-like linespread function (LSF) during observations. A more detailed description of the instrument can be found in Delorme et al. (2021) and Wang et al. (2021).

Our KPIC observations of the HIP 99770 b are summarized in Table 2. We used an AB nodding scheme that alternately aligns the companion on one of two fibers to facilitate sky/background subtraction. Eighteen frames of 300 s exposure time were recorded on June 16 and 11 exposures of 600 s on June 21. The total integration time on HIP 99770 b was 90 and 60 minutes, respectively. We also switched to the primary star once every hour for modeling telluric absorption and instrument response. Each night we took short observations on an M giant star, HIP 95771 and HIP 81497, respectively, which display deep and narrow spectral lines, therefore convenient for the calibration of the wavelength solution.

We reduced the data using the public KPIC Data Reduction Pipeline, 16 including steps of nod subtraction, bad pixel removal, spectral order tracing, optimal spectrum extraction, and wavelength calibration. We refer readers to Wang et al. (2021) for an in-depth description. The *K*-band observations span the wavelength range of $1.9-2.5\,\mu\text{m}$, with a spectral resolution of $\mathcal{R}\sim35,000$. We focused our analysis on the three reddest spectral orders from 2.29 to 2.49 μm , covering the main near-infrared absorbing molecules such as CO and H_2O in the companion's atmosphere, as shown in Figure 1.

As a result of the companion's small separation (0".44) and high contrast ($\Delta K_{\rm mag} = 11.3$), the extracted spectra are dominated by the diffracted starlight, which varies across wavelengths. Therefore, the continuum of the companion's spectrum cannot be recovered. Taking into account the photon noise from the stellar speckles, we reach an S/N of ~ 1 pixel⁻¹ for the companion's signal in 1.5 hr integration on the first night and S/N ~ 0.8 pixel⁻¹ on the second night.

4. Retrieval Analysis

4.1. Spectral Model of HIP 99770 b

The spectral model of the companion consists of three components: the temperature profile, the chemistry model, and the cloud model. The models are set up as follows.

4.1.1. Temperature Model

We parameterize the temperature–pressure (T-P) profile using the gradients $\Delta \ln T/\Delta \ln P$ across seven pressure knots

¹⁶ https://github.com/kpicteam/kpic_pipeline

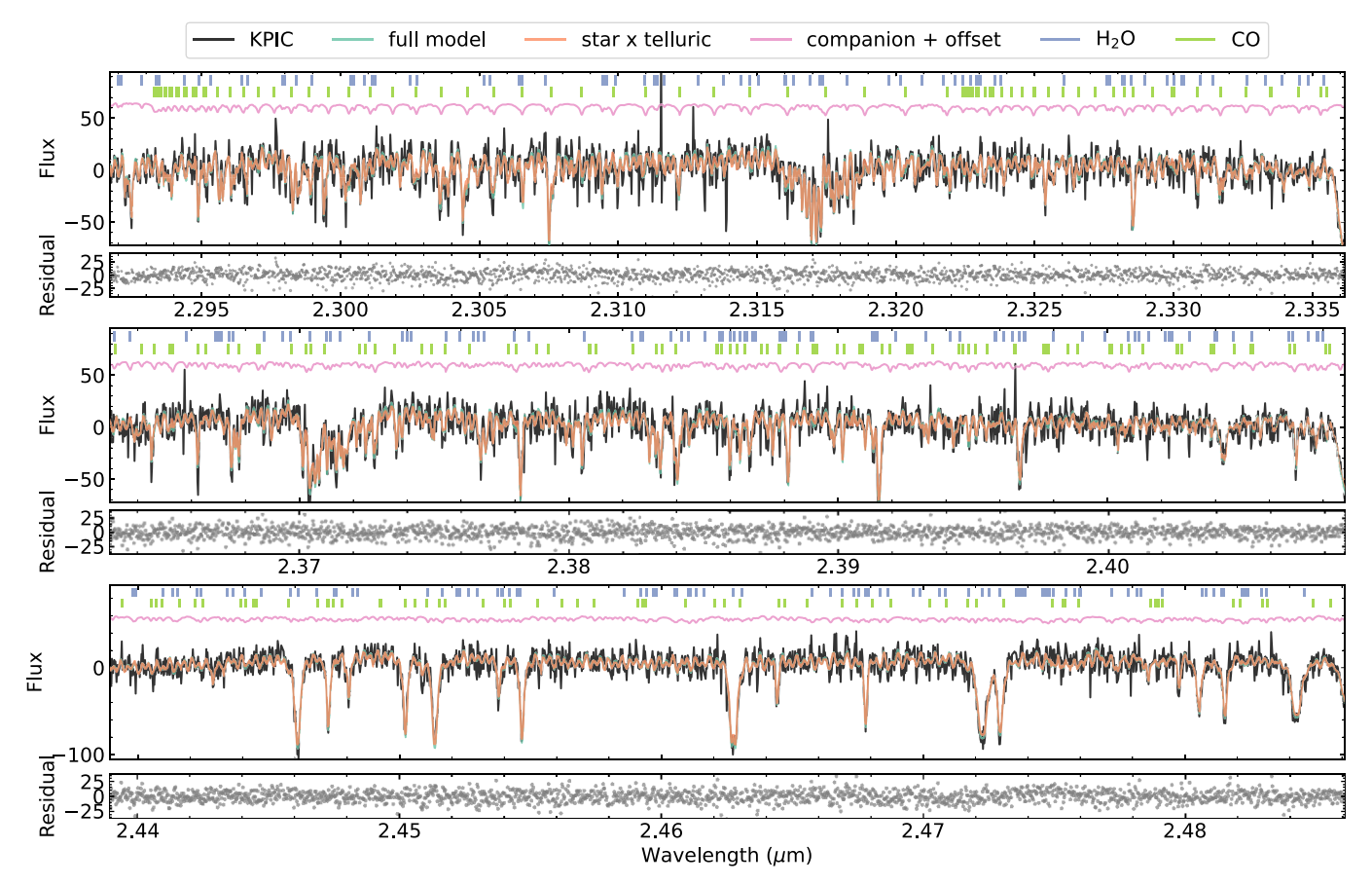


Figure 1. High-pass-filtered K-band (2.29–2.49 μ m) spectra of the HIP 99770 system taken with one of KPIC fibers. The observations are shown with black lines. Overplotted is the best-fit full model as obtained with the retrieval analysis. The spectrum is dominated by the stellar contribution, with a small fraction of emission from the companion, as shown in the offset pink lines. We annotated the positions of absorption features from H_2O and H_2O

set at 10^{-5} , $10^{-3.5}$, 10^{-2} , 10^{-1} , 10^{0} , 10^{1} , and 10^{2} bars and one absolute temperature value, T_0 , at 100 bars. This follows the approach in Zhang et al. (2023) and Xuan et al. (2024b). We set broad prior ranges with a uniform distribution to ensure the flexibility of the temperature model (see Table 3). The full T-P profile is determined by a spline interpolation onto 60 layers evenly spaced in log pressure between 10^{-5} and 100 bars.

4.1.2. Chemistry Model

We explore two different chemistry models: one a free retrieval and the other a disequilibrium model. The disequilibrium chemistry model first assumes chemical equilibrium to determine the chemical abundances at a given pressure, temperature, carbon-to-oxygen ratio (C/O), and metallicity ([M/H]), by interpolation of a precomputed table (Mollière et al. 2017, 2020). The model then parameterizes the disequilibrium chemistry of major species (CO, CH₄, and H₂O) by enforcing constant volume mixing ratios (VMRs) at altitudes above a certain quenching pressure level (P_{quench}), which approximates the effect of rapid vertical mixing in disequilibrium chemistry (Zahnle & Marley 2014). The free chemistry model allows the abundance of each chemical species to vary while assuming a vertically constant profile. In the case of chemical quenching at a deep atmospheric region below the photosphere and modest vertical sampling of the atmosphere, this constant VMR profile can be a reasonable

approximation, which is therefore expected to lead to similar retrieval results to the disequilibrium chemistry model.

4.1.3. Cloud Model

We adopt the condensate cloud model from Ackerman & Marley (2001), with MgSiO₃ as the cloud opacity source—the expected dominant cloud species in L dwarfs (Cushing et al. 2006). The cloud is characterized by four parameters: the mass fraction of the cloud species at the cloud base $X_0^{\text{MgSiO}_3}$, the settling parameter f_{sed} (controlling the thickness of the cloud above the cloud base), the vertical eddy diffusion coefficient K_{zz} (effectively determining the particle size), and the width of the lognormal particle size distribution σ_g . Following Mollière et al. (2020), the location of the cloud base P_{base} is determined by intersecting the condensation curve of the cloud species with the T-P profile of the atmosphere.

4.2. Fringing Removal

Inspecting the observational residuals, i.e., the observed spectra minus the best-fit model as obtained through the retrieval analysis, we identified sinusoidal fringing features in the data. These fringing signals are believed to result from the entrance window of NIRSPEC and KPIC dichroics. Although the fringing due to the NIRSPEC entrance window is static, the KPIC fringing signal shows temporal variation depending on the angle of incidence into the optics and the change of optical properties of the material with ambient temperature (Finnerty et al. 2022).

Table 3Priors and Posteriors of the Retrievals

Parameter	Prior	Disequilibrium	Free
$M_p (M_{\text{Jup}})$	N(16.1, 5.0)	17.2 ± 4.2	17.3 ± 4.2
$R_p (R_{\rm Jup})$	U(0.7, 1.3)	$0.94^{+0.21}_{-0.16}$	$0.93^{+0.22}_{-0.15}$
$v \sin i \text{ (km s}^{-1})$	U(0.1, 20)	$3.5^{+1.7}_{-1.9}$	$3.4^{+1.7}_{-1.9}$
$RV (km s^{-1})$	U(-30, 30)	17.9 ± 0.3	17.9 ± 0.3
$\epsilon_{ m limb}$	$\mathcal{U}(0, 1)$	0.5 ± 0.3	0.5 ± 0.3
$\mathcal{R}_{ ext{scaling}}$	U(0.8, 1.2)	$0.96^{+0.12}_{-0.10}$	$0.95^{+0.12}_{-0.10}$
[M/H]	U(-1.5, 1.5)	$0.26^{+0.24}_{-0.23}$	0.22 ± 0.23
C/O	U(0.1, 1.5)	$0.55^{+0.06}_{-0.04}$	0.64 ± 0.05
$\log X^{\mathrm{H_2O}}$	U(-12, -1)		-2.47 ± 0.21
$\log X^{\rm CO}$	U(-12, -1)	•••	-2.03 ± 0.23
$\log X^{\mathrm{CH_4}}$	U(-12, -1)	•••	$-5.2^{+0.6}_{-4.4}$
$\log X^{\mathrm{NH_3}}$	U(-12, -1)	•••	$-7.5^{+2.5}_{-2.9}$
$\log X^{13}CO$	U(-12, -1)		$-4.5^{+0.6}_{-4.2}$
$\log(^{13}\mathrm{CO}/^{12}\mathrm{CO})$	U(-12, -1)	$-2.7^{+0.8}_{-5.6}$	•••
$logP_{quench}$ (bars)	U(-5, 2)	$0.21^{+1.06}_{-0.83}$	•••
T_0 (K)	U(1500, 5000)	3904 ± 785	4094 ± 724
$(d \ln T/d \ln P)_0$	U(0.02, 0.05)	0.035 ± 0.01	0.035 ± 0.01
$(d \ln T/d \ln P)_1$	U(0.03, 0.07)	0.05 ± 0.01	0.05 ± 0.01
$(d \ln T/d \ln P)_2$	U(0, 0.15)	0.07 ± 0.05	0.08 ± 0.05
$(d \ln T/d \ln P)_3$	U(0, 0.5)	0.22 ± 0.09	0.29 ± 0.12
$(d \ln T/d \ln P)_4$	U(0., 0.5)	0.12 ± 0.05	0.13 ± 0.06
$(d \ln T/d \ln P)_5$	U(0.,0.5)	0.22 ± 0.10	0.24 ± 0.09
$(d \ln T/d \ln P)_6$	U(0, 0.5)	0.20 ± 0.15	0.17 ± 0.14
$\log(X_0^{\mathrm{MgSiO_3}})$	U(-12, -1)	-7.4 ± 3.0	-7.4 ± 3.0
$f_{\rm sed}$	U(0, 10)	6.0 ± 2.5	6.0 ± 2.5
$\log(K_{zz})$	U(5, 13)	6.0 ± 2.6	6.0 ± 2.6
σ_g	<i>U</i> (1.05, 3)	2.0 ± 0.6	2.0 ± 0.6

Note. $\mathcal{U}(a, b)$ represents a uniform distribution, and $\mathcal{N}(a, b)$ represents a normal distribution. The last two columns show posteriors with 1σ uncertainties from the disequilibrium chemistry model and free chemistry model.

We found significant fringing in the periodogram of the residual data, with a period of \sim 4.5 Å originating from the KPIC dichroics, especially in the second epoch. To model the fringing, we used the function as described in Xuan et al. (2024b):

$$t = \left[1 + F\sin^2\left(\frac{2\pi nd}{\lambda}\right)\right]^{-1},\tag{1}$$

where n is the index of refraction of the material as a function of wavelength λ . F and d are two free parameters determining the amplitude and period of the fringing signal. We fit this function to the observational residuals using least-squares optimization to obtain the optimal fringing parameters in each spectral order and fiber. Then, we applied this optimized fringing formula to the full spectral model during retrieval analysis. We note that the fringing signals do not bias the measurement of chemical composition, as we obtained consistent results either with or without the treatment of fringing.

4.3. Retrieval Framework

Given the model setup detailed in Section 4.1, we compute synthetic spectra of the companion using the radiative transfer code petitral TRANS (pRT; Mollière et al. 2019). The model accounts for the Rayleigh scattering of H_2 and H_2 , the

collision-induced absorption of H_2-H_2 and H_2-H_e , and the scattering and absorption cross sections of crystalline, irregularly shaped MgSiO₃ cloud particles. We use the line-by-line mode of pRT to calculate the emission spectra at high spectral resolution. To speed up the calculation, we downsample the original opacity tables (with $\lambda/\Delta\lambda\sim 10^6$) by a factor of 3. This downsampling factor has been tested to ensure that it does not bias the retrieval results (Zhang et al. 2021a; Xuan et al. 2022). We include opacity from H_2O (Polyansky et al. 2018), ^{12}CO , ^{13}CO (Li et al. 2015), CH₄ (Hargreaves et al. 2020), CO₂ (Rothman et al. 2010), and NH₃ (Coles et al. 2019) in our model.

Subsequently, the synthetic high-resolution spectrum is radial velocity (RV) shifted by the systemic and barycentric velocity and rotationally broadened by $v \sin i$ using the method from Carvalho & Johns-Krull (2023). The model spectrum at native resolution is then convolved with a Gaussian kernel and binned to the wavelength grid of the observed spectrum to match the resolving power of the instrument ($\lambda/\Delta\lambda \sim 35{,}000$). The width of the LSF is measured from the point-spread function of the stellar observations in the cross-dispersion direction. We apply a scaling factor $\mathcal{R}_{scaling}$ to the width to account for potential inaccuracy in the measured values. Then, the model spectrum is multiplied by the telluric transmission and instrument response, which is obtained by dividing the spectrum of the featureless A-type primary star by a PHOENIX stellar model (Husser et al. 2013). As the spectrum is contaminated by low-order stellar speckle noise, we discard the continuum information by high-pass filtering of both the observation and model using a 150-pixel (\sim 3 nm) wide Gaussian filter. We note that the retrieval results are robust to the choice of the kernel width.

To construct the full forward model and compare it directly to observations, we took the linear combination of the companion's component m_p with the observed stellar spectrum m_* following Ruffio et al. (2019), Wang et al. (2021), and Landman et al. (2024). The full model is calculated as follows:

$$M = m c = \begin{bmatrix} m_* & m_p \end{bmatrix} \begin{bmatrix} c_* \\ c_p \end{bmatrix}, \tag{2}$$

where the coefficients c of the two linear components can be analytically marginalized by solving the linear equation

$$d = m c + \eta, \tag{3}$$

with d being the observed spectrum and η the random noise. The least-squares solution for the linear equation can be found by solving

$$\boldsymbol{c}^T \boldsymbol{m}^T \Sigma_0^{-1} \boldsymbol{m} = \boldsymbol{d}^T \Sigma_0^{-1} \boldsymbol{m}, \tag{4}$$

where Σ_0 is the covariance matrix, with the diagonal items populated by observation uncertainties. Here we do not account for the nondiagonal covariance matrix because of the low S/N of the observations. We test for the effects of correlated errors by modeling them with Gaussian processes (GPs) following de Regt et al. (2024) and find no difference in the constraints on the free parameters (see Figure 9 in the Appendix). This demonstrates that the uncorrelated noise dominates the uncertainty.

The log-likelihood of the model M is formulated as

$$\ln \mathcal{L} = -\frac{1}{2} [N \ln(2\pi) + \ln(|\Sigma_0|) + N \ln(s^2) + \frac{1}{s^2} (\mathbf{d} - \mathbf{M})^T \Sigma_0^{-1} (\mathbf{d} - \mathbf{M}) \right],$$
 (5)

where N is the number of data points and s is an error bar inflation parameter, which accounts for the underestimated uncertainties of the observations. Following Ruffio et al. (2019), the optimal s for each model can be calculated by effectively scaling the reduced χ^2 to 1:

$$s^2 = \frac{1}{N} (\boldsymbol{d} - \boldsymbol{M})^T \Sigma_0^{-1} (\boldsymbol{d} - \boldsymbol{M}).$$
 (6)

The error bar inflation parameter can essentially account for the model's systematic errors compared to the observations, which ensures that these uncertainties are propagated to the posteriors of the free parameters. The log-likelihood is evaluated in each spectral order and fiber before being combined, allowing for different linear coefficients and error bar inflation factors optimized for each order.

In total, the retrieval with the disequilibrium chemistry model has 22 free parameters, and the free chemistry model has 23 free parameters, as summarized in Table 3. For the Bayesian inference process, we use the nested sampling tool PyMultiNest (Buchner et al. 2014), which is a Python wrapper of the MultiNest method (Feroz et al. 2009). The retrievals are performed in importance nested sampling mode with a constant efficiency of 5%. It uses 2000 live points to sample the parameter space and derives the posterior distribution of free parameters.

5. Retrieval Results

We jointly fit two epochs of KPIC observations by generating the model spectrum, calculating the likelihood for each epoch, and summing up the two likelihood values. We show retrieval results for two model setups: disequilibrium and free chemistry. The posterior distributions of the free parameters in these models are summarized in Table 3. In general, these models result in consistent constraints on the atmospheric properties. We also carry out analyses for the two epochs independently. The retrieved parameters are consistent within 1σ – 2σ , as shown in Figure 8. The first epoch provides slightly tighter constraints because of its better S/N (see Table 2).

5.1. Cross-correlation Detection

We carried out a cross-correlation analysis to show the detection of molecules in HIP 99770 b. The cross-correlation functions (CCFs) were computed as

$$CCF(v) = \frac{1}{s^2} \mathbf{F}(v)^T \Sigma_0^{-1} \mathbf{R}, \tag{7}$$

where R is the observed spectra minus the best-fit disequilibrium chemistry model, with the abundance of a specific molecule being set to zero; F is the molecular template that was computed by differencing the best-fit model and the best-fit model without the contribution of that molecule; and v is the RV shift between the model and data. Both R and F were high-

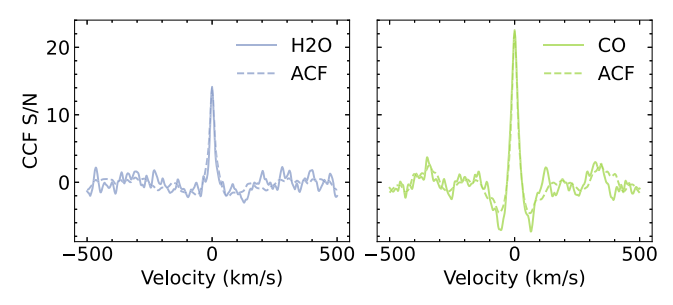


Figure 2. Cross-correlation detection of H_2O and CO in KPIC observations of HIP 99770 b. The CCFs are scaled by the noise to show the detection S/N on the y-axis. The dashed lines show the ACF of each molecular template.

pass filtered using a median filter with a width of 100 pixels. Then, the CCFs of individual orders were combined into a master CCF, as shown in Figure 2. The noise of the CCF was estimated by subtracting the model's autocorrelation function (ACF) and taking the standard deviation at $|\nu| > 150 \, \mathrm{km \, s^{-1}}$. We detected H₂O and CO with an S/N of 14 and 23, respectively. We checked other molecules, including CH₄, NH₃, ¹³CO, H₂S, and CO₂, and found no significant detections (see Figure 7 in the Appendix).

5.2. C/O and Metallicity

The retrieved chemical abundances and metallicity [M/H] and C/O ratios using two models are shown in Figure 3. Using the disequilibrium chemistry model, we obtained a C/O = $0.55^{+0.06}_{-0.04}$ and [M/H] = $0.26^{+0.24}_{-0.23}$ (1 σ confidence intervals). The empirical level of systematic uncertainty of KPIC measurements is $\sim 20\%$ for C/O ratio and 0.2 dex for metallicity, as estimated from benchmark brown dwarf companions, HR 7672 B and HD 4747 B (Wang et al. 2022; Xuan et al. 2022). These are roughly consistent with our results on HIP 99770 b. The free chemistry model resulted in a derived C/O of 0.64 ± 0.05 and a metallicity of 0.22 ± 0.23 , in line with the disequilibrium chemistry model. In comparison, the free chemistry model retrieved consistent VMRs for the major molecules as shown in Figure 3. The slightly different C/O ratio derived from the free chemistry model can be attributed to the cold trapping of oxygen in clouds (Woitke et al. 2018). Condensates such as MgSiO₃ take a fraction of oxygen out of the gas phase. The chemical model predicts a mass fraction of $\sim 2.4 \times 10^{-3}$ for MgSiO₃, which was not constrained with our analysis (see Section 5.4). Taking this amount of clouds into account, we estimated that the actual C/O ratio in the free chemistry model would be ~ 0.55 , consistent with the result from the disequilibrium chemistry model.

Regarding Bayesian evidence, the disequilibrium chemistry model slightly outperforms the free chemistry model at 3σ significance (Benneke & Seager 2013). The values are summarized in Table 4. We found that the log-likelihood of the best-fit disequilibrium model is the same as the free chemistry model. This suggests that both models fit the observations equally well, and the slightly lower Bayesian evidence of the free chemistry model is due to the increased number of free parameters. Additionally, we tested imposing a Gaussian prior of $1.1 \pm 0.1~R_{\rm Jup}$ on the radius of the companion following the evolutionary model (Baraffe et al. 2003; Currie et al. 2023) and found that the retrieval results remained entirely consistent.

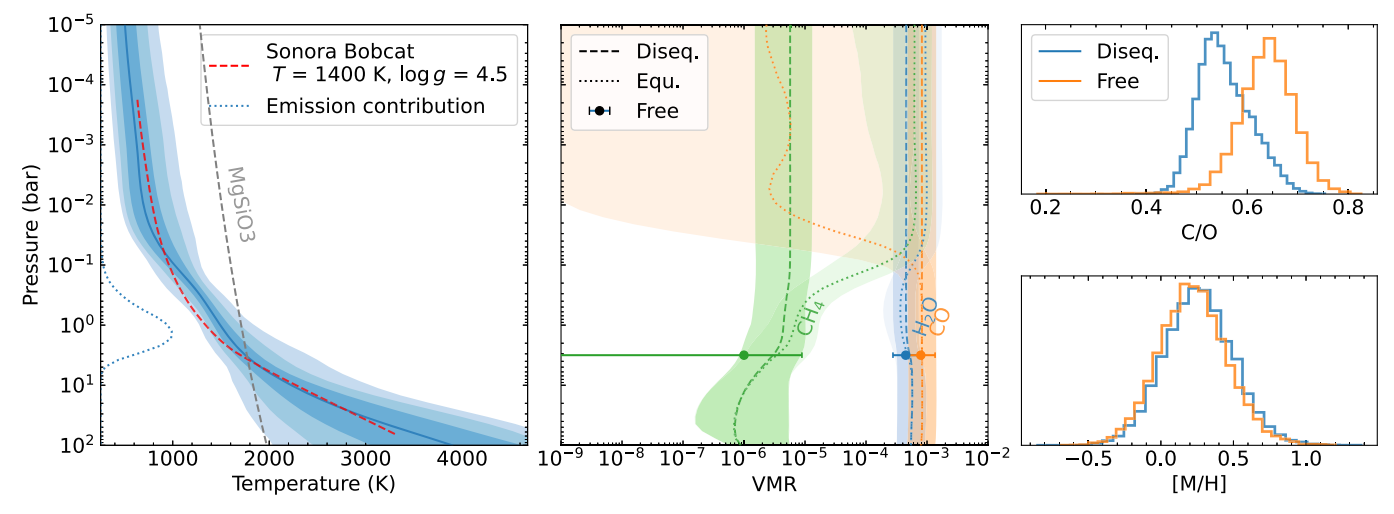


Figure 3. Retrieved temperature structure and chemical abundances of HIP 99770 b. Left panel: best-fit T-P profile, with 1σ , 2σ , and 3σ envelope shown in blue. The red dashed line is the self-consistent T-P profile of $T_{\rm eff} = 1400$ K and $\log g = 4.5$ from the Sonora model (Marley et al. 2021). The blue dotted line represents the flux-weighted emission contribution of the model. The gray dashed line shows the condensation curve of the MgSiO₃ cloud. Middle panel: retrieved VMRs of the major molecules with 1σ envelopes. The dashed lines show the results of the disequilibrium chemistry model; the dotted lines represent the equilibrium case when the chemical quenching is manually turned off. The error bars denote the retrieved VMRs in the free chemistry model. Right panels: comparison of the retrieved C/O and metallicity of the disequilibrium and free chemistry models. The free chemistry model retrieves a slightly higher C/O ratio because of the hidden oxygen in cloud condensates, such as enstatite.

Table 4
Summary of Bayesian Evidence of Various Retrieval Models

Model	$\ln Z$	$\Delta \ln Z$	Significance (σ)
Disequilibrium chemistry	-93748.5		•••
Free chemistry	-93751.8	-3.3	3.1
Equilibrium chemistry	-93750.0	-1.5	2.4
Disequilibrium chemistry, no cloud	-93746.2	2.3	2.7

Note. $\Delta \ln Z$ represents the difference of Bayesian evidence $\ln Z$ of each alternative model compared to the nominal disequilibrium chemistry model.

5.3. Disequilibrium Chemistry

The disequilibrium chemistry model retrieves a quench pressure of $P_{\rm quench} \sim 0.2$ –22.4 bars (1σ) . This quench pressure is needed in order to explain the observed underabundance of CH₄ relative to CO in the atmosphere. In contrast, turning off chemical quenching results in a transition from a CO-dominated to a CH₄-dominated composition at pressures below 0.1 bars given the T-P profile (see Figure 3). The KPIC observations do not support this equilibrium case, as the VMR of CO in our free chemistry retrieval is constrained to a higher value than the equilibrium prediction, and we obtain a 3σ upper limit of $<4\times10^{-5}$ on the VMR of CH₄.

We reran the retrieval assuming chemical equilibrium without quenching and compared the resulting fit to the nominal model with quenching. The equilibrium retrieval converged to a more isothermal T-P profile (i.e., hotter upper layers) in order to avoid the transition to a CH₄-dominated atmosphere. We calculated the Bayes factor for these two models and found that the nominal disequilibrium chemistry model is favored over that for equilibrium at a 2.4σ significance. Similar findings have been observed in several late L-type super-Jupiters such as HR 8799 cde (e.g., Konopacky et al. 2013; Barman et al. 2015; Mollière et al. 2020) and brown dwarfs (e.g., Xuan et al. 2022; de Regt et al. 2024).

5.4. Clouds

The cloud-related parameters were not constrained in our retrieval analysis (see Table 3 and Figure 6). We calculated the Bayesian evidence for the clear versus cloudy models and found that the clear model is slightly preferred at 2.7σ significance because of fewer free parameters. We retrieved consistent chemical abundances from the cloudy and cloud-free models. While clouds are expected in atmospheres of late L-type brown dwarfs (Burrows et al. 2006), the reason for our data's insensitivity to clouds may be twofold. First, the limited S/N of the observations may not be sufficient to distinguish the small differences in line contrasts caused by the cloud opacity. Second, the silicate cloud base in our model is located at \sim 10 bars, below the photosphere of the atmosphere in K band, as shown in Figure 3. Hence, the impact of cloud opacity is not significant at the pressure levels probed by the high-resolution K-band observations (see also Zhang et al. 2021a; Xuan et al. 2022; Inglis et al. 2024; Landman et al. 2024).

5.5. Rotation and RV

The projected rotation velocity of HIP 99770 b is measured to be $v\sin(i) = 3.5^{+1.7}_{-1.9}\,\mathrm{km\,s^{-1}}$ in our retrievals. However, considering the spectral resolution of KPIC ($\mathcal{R}\sim35,000$), the instrument broadening dominates over the rotational broadening of the target, meaning that the rotation is not resolved in our data. The likelihood of the best-fit retrieval model shows no difference whether including spin as a free parameter or not. Therefore, we report a 3σ upper limit of $v\sin(i) < 7.8\,\mathrm{km\,s^{-1}}$ as derived from the posterior distribution. This is also consistent with the spectral resolution of KPIC. Adopting an isotropic distribution of inclination, we estimated its spin velocity to be $<10\,\mathrm{km\,s^{-1}}$, which corresponds to a rotation velocity versus breakup velocity $v/v_{\mathrm{break}} \sim 0.06$. We further discuss this constraint in Section 6.1.

We measured an RV of -17.9 ± 0.3 km s⁻¹ for HIP 99770 b. This allows us to compute the relative RV between the star and companion and add to the orbital constraints of the system.

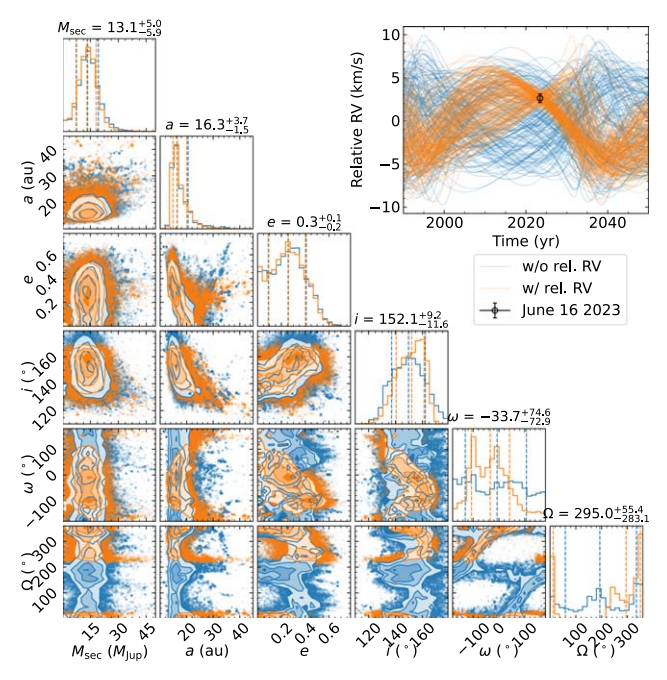


Figure 4. Comparison of the orbital fitting of the HIP 99770 system with and without the relative RV measurement in orange and blue, respectively. The corner plot shows posterior distributions of parameters such as the companion's mass $M_{\rm sec}$, semimajor axis a, eccentricity e, inclination i, argument of periastron ω , and longitude of ascending node Ω . The upper right panel shows the relative RV over time from random draws of the orbital solutions in both fits. Adding our RV measurement to the fitting helps improve constraints on i, ω , and Ω . The updated 1σ constraints are labeled on top of each column.

Since the A-type host star is almost featureless in K band, we cannot measure the stellar RV in our KPIC data. The stellar RV is not fully consistent in the literature, likely because the fast rotation of the star (\sim 80 km s⁻¹; Gaia Collaboration et al. 2021) makes it challenging to measure the RV accurately. We adopted the RV measurement of HIP 99770 from Gaia DR3 of $-20.5 \pm 0.4 \,\mathrm{km \, s^{-1}}$ (Gaia Collaboration et al. 2021). This led to a relative RV of $2.6 \pm 0.5 \,\mathrm{km \, s^{-1}}$ between the companion and primary. Adding this relative RV constraint, we carried out orbital fitting using the orvara code (Brandt et al. 2021) following Currie et al. (2023) to refine the orbital properties of HIP 99770 b. We note that here we used the default $1/M_{\rm sec}$ prior for the secondary mass, which is responsible for the lower $M_{\rm sec}$ (~13 $M_{\rm Jup}$) as was also mentioned in Currie et al. (2023). We compared the posteriors of the orbital fitting with and without the relative RV measurement in Figure 4. Although the addition of relative RV did not significantly change the overall orbital constraints, it assisted in ruling out some solutions and improving the constraint on the argument of periastron ω , longitude of ascending node Ω , and orbital inclination $i = 152^{+9}_{-11}$ deg. Additional epochs of RV measurements in a 5 yr baseline will further strengthen the constraining power on other parameters, such as the secondary mass and orbital eccentricity.

6. Discussion

6.1. Rotation Velocity

Putting our upper limit on rotation velocity into context, we note that the spin of HIP 99770 b is at the low end compared to literature measurements of other super-Jovian companions as shown in Figure 5. Previous studies suggest that younger

companions generally have lower rotation rates, which are expected to increase with age as their radii contract following angular momentum conservation (Bryan et al. 2020b; Vos et al. 2020). In contrast, field brown dwarfs display a larger scatter in spin (Hsu et al. 2021). Although the age of HIP 99770 b is older than 40 Myr, its rotation velocity (assuming isotropic inclination distribution) is comparable to that of very young companions (<10 Myr), such as GQ Lup b (Schwarz et al. 2016), DH Tau b, and HIP 79098 b (Xuan et al. 2024a), and is lower than those at older ages. If the trend of increasing spin with increasing age holds, it may indicate a nearly pole-on orientation for HIP 99770 b. If we assume that its spin and orbit are aligned ($i \sim 152$), the spin velocity is <15 km s⁻¹ or $v/v_{\rm break} \sim 0.09$, making it more comparable to other super-Jovian companions.

On the other hand, the slow spin may be indicative of effective magnetic braking by the circumplanetary disk (CPD; Batygin 2018; Ginzburg & Chiang 2020; Wang et al. 2021). Massive companions are expected to effectively ionize the CPD, and interactions with magnetic fields then act to spin down the companions. Therefore, the slow spin of HIP 99770 b may indicate that it hosted an unusually long-lived CPD and/or that it formed early via gravitational instability, both of which allow for a longer time for the companion to spin down. The large scatter in the measured spins of super-Jupiter companions may represent the consequences of mixed formation pathways and histories (Bryan et al. 2020b). Future rotation period measurements with light curves will help break this degeneracy with inclination. More accurate measurements of rotation velocities using high-resolution, large spectral grasp instruments such as VLT/CRIRES⁺ and Keck/HISPEC will be essential for understanding the population-level trend.

6.2. Implication for Formation

We retrieve an atmospheric $[M/H] = 0.26 \pm 0.24$ and $C/O = 0.55 \pm 0.06$ (1σ confidence intervals) for HIP 99770 b, consistent with the solar values. Previous studies reported stellar abundances of $[C/H] \sim 0.18 \pm 0.09$ and $[O/H] \sim 0.01 \pm 0.09$ (Erspamer & North 2003; Hinkel et al. 2014). This corresponds to a C/O ratio of $0.8^{+0.3}_{-0.2}$, roughly consistent with a solar to supersolar value of 0.59 ± 0.08 (Asplund et al. 2021). The uncertainties in the stellar composition result from the large rotational broadening of the primary and the deficit of oxygen lines in its spectrum. A more accurate stellar C/O constraint is needed in order to draw unambiguous conclusions on the formation of the companion. For consistency, we simply assume a solar composition for the primary star HIP 99770 in the following discussion.

The companion's current semimajor axis of 17 au is well within the typical location of the CO ice line in protoplanetary disks around early-type stars (Qi et al. 2015). This makes it an interesting case for testing formation models. Given our constraints on its atmospheric composition, the companion is compatible with a formation via either core accretion or gravitational instability. Based on the static picture of chemistry in smoothed protoplanetary disks (Öberg et al. 2011), the core accretion scenario is expected to result in (1) a substellar C/O and metal-rich atmosphere because of the accretion of oxygen-enhanced solids, (2) an elevated C/O combined with substellar metallicity due to gas-dominated accretion, or (3) a stellar C/O when the accreted material corresponds to an overall stellar metallicity for the atmosphere.

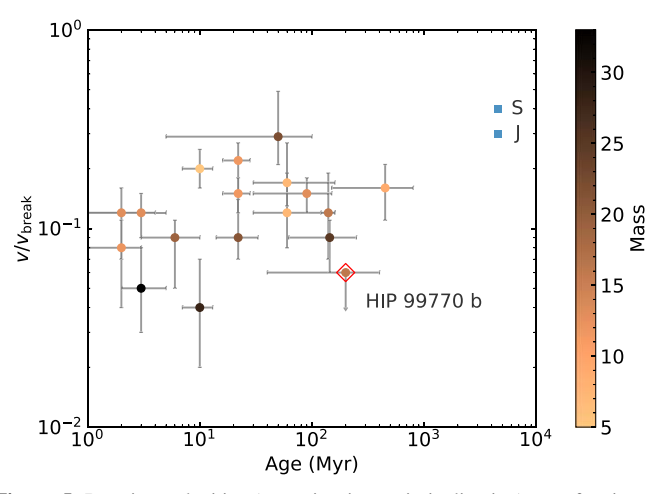


Figure 5. Rotation velocities (assuming isotropic inclination) as a fraction of breakup velocities for super-Jovian companions. Our measurement of HIP 99770 b is denoted with a red diamond. The measurements of other companions are adopted from the literature, including Bryan et al. (2020b), Wang et al. (2021), and Xuan et al. (2024a). The data are color-coded by the companion masses. The blue data points show the spin of Jupiter and Saturn in the solar system.

In practice, protoplanetary disks are not static and have complicated substructures (Öberg et al. 2021). Dust drift and chemical evolution of gas and dust can alter the distribution of disk elemental abundances over time (Mollière et al. 2022). Planet formation models coupled with disk chemistry evolution and dust migration are needed to investigate these questions further. Qualitatively, disk observations support the simplified picture that the gas-phase oxygen is strongly depleted as more O-bearing species are locked in the ice phase beyond the snowline (Bosman et al. 2021; Le Gal et al. 2021). Therefore, planets formed under such conditions are expected to follow the scenarios outlined above.

In contrast, gravitational instability should lead to similar stellar and companion atmospheres since it is thought to occur relatively early, when the disk is massive and the reservoir of solids is pristine (Schib et al. 2021). Although the companion may undergo late enrichment by solid accretion after the initial collapse, this would not significantly alter the composition, due to the high envelope mass; for example, to enhance the metallicity by 1 dex would require accreting $\sim 2 M_{\rm Jup}$ of solids (Inglis et al. 2024). Similarly, we do not expect a large enrichment of metal in super-Jupiter atmospheres in core accretion models. Therefore, the solar composition of HIP 99770 b does not preclude either formation scenario. If the companion was born ex situ, it may have formed in the outer disk followed by type II migration (Dürmann & Kley 2015; Robert et al. 2018). Such planet migration could potentially boost the accretion of planetesimals, leading to a slight metal enrichment, as we constrain for HIP 99770 b.

The chemical composition of HIP 99770 b also fits in the overall trend for super-Jupiter companions. Xuan et al. (2024a) carried out retrieval analyses in a sample of 10–30 $M_{\rm Jup}$ companions using KPIC observations. They found that the companions generally had solar compositions, hinting at formation via gravitational collapse or plausible core accretion beyond the CO ice line. In contrast, lower-mass (<10 $M_{\rm Jup}$) companions appear to display a larger range in C/O and metallicity (e.g., Whiteford et al. 2023; Zhang et al. 2023; Landman et al. 2024; Nasedkin et al. 2024). By comparing the

C/O ratio in a sample of directly imaged companions with transiting exoplanets, Hoch et al. (2023) suggested that there are two distinct populations with a boundary at $\sim 5 M_{\rm Jup}$, implying a transition of formation pathways near a mass range of 5-10 M_{Jup} . However, more work is needed to determine whether there exists a clear mass boundary for distinct formation channels, as such compositional measurements get challenging toward lower-mass and closer-in companions. The comparison between directly imaged super-Jupiters and transiting exoplanets with similar masses will be informative in distinguishing whether these populations are separated by different formation pathways or migration histories (Kempton & Knutson 2024). It also calls for the joint understanding of trends in the orbital architectures of these systems (Nielsen et al. 2019; Bowler et al. 2020; Do Ó et al. 2023; Nagpal et al. 2023) to unravel their formation.

7. Conclusion

We carried out detailed spectral characterization of the recently discovered super-Jupiter companion HIP 99770 b using the fiber-fed high-resolution spectrograph KPIC ($\mathcal{R} \sim 35,000$). The K-band observations led to clear detections of H₂O and CO in the atmosphere of HIP 99770 b. We used atmospheric retrievals to constrain its atmospheric composition, including its C/O, metallicity, projected rotation velocity ($v \sin i$), and RV.

- 1. We found that the companion's atmosphere has $C/O = 0.55 \pm 0.06$ and $[M/H] = 0.26 \pm 0.24$ (1σ confidence interval), which are consistent with stellar values. It joins the ensemble of super-Jovian companions showing broadly solar compositions. This is compatible with a formation via either gravitational instability or core accretion.
- 2. We found that the ratio of CH₄ to CO in the companion's atmosphere is lower than predicted by equilibrium chemistry models, and we place a lower bound of 0.2 bars on the quench pressure.
- 3. Although the companion is expected to be cloudy, we found that our models do not require clouds. This may be because of the limited S/N, or because the clouds are located below the photosphere for our *K*-band observations. The presence or absence of clouds could be better constrained by expanding the wavelength range of these observations, which would increase our sensitivity to the wavelength-dependent scattering signal from clouds.
- 4. We added the companion-to-primary relative RV measurement to the orbital fitting and obtained updated constraints on the companion's orbital $i, \, \omega,$ and $\Omega.$
- 5. The projected rotation velocity $v \sin(i) < 7.8 \text{ km s}^{-1}$ is small compared to other directly imaged companions with similar ages and masses. This may indicate a nearly pole-on orientation or effective magnetic braking by a CPD.

Located within 20 au and straddling the deuterium-burning mass boundary, HIP 99770 b represents an intriguing target to investigate the link between the present atmosphere and formation history. The convoluted formation and evolution processes make it challenging to retrace the origin of planets unambiguously. Modeling studies on the formation of these well-characterized super-Jovian companions are crucial for advancing our knowledge. In the future, higher-S/N spectroscopic observations will

allow for tighter constraints on the metallicity by probing elements beyond C and O. The estimates of solid budgets will massively benefit the inference of formation history (Lothringer et al. 2021; Chachan et al. 2023). Other formation tracers, such as carbon isotope ratios, will help pin down the formation location relative to the CO ice line, therefore allowing us to lift the degeneracy between formation mechanisms (Zhang et al. 2021b). Detailed characterization of similar companions will play an essential role in understanding the formation of the super-Jovian population, spanning a wide range of properties.

Acknowledgments

Y.Z. is thankful for support from the Heising-Simons Foundation 51 Pegasi b Fellowship (grant No. 2023-4298). Y.C. acknowledges support from the Natural Sciences and Engineering Research Council of Canada (NSERC) through the CITA National Fellowship and the Trottier Space Institute through the TSI Fellowship. Funding for KPIC has been provided by the California Institute of Technology, the Jet Propulsion Laboratory, the Heising-Simons Foundation (grant Nos. 2015-129, 2017-318, 2019-1312, and 2023-4598), the Simons Foundation, and the NSF under grant AST-1611623. The data presented herein were obtained at the W. M. Keck Observatory, which is operated as a scientific partnership among the California Institute of Technology, the University of California, and the National Aeronautics and Space Administration. The Observatory was made possible by the generous financial support of the W. M. Keck Foundation. The authors

wish to recognize and acknowledge the very significant cultural role and reverence that the summit of Maunakea has always had within the indigenous Hawaiian community. We are most fortunate to have the opportunity to conduct observations from this mountain. The computation was carried out on the Caltech High Performance Cluster.

Facility: Keck:II (KPIC)

Software: numpy (Harris et al. 2020), scipy (Virtanen et al. 2020), matplotlib (Hunter 2007), astropy (Astropy Collaboration et al. 2018), petitRADTRANS (Mollière et al. 2019), PyMultiNest (Buchner et al. 2014), orvara (Brandt et al. 2021), corner (Foreman-Mackey 2016),

Appendix Retrieval Results

We summarize the Bayesian evidence of various retrieval models mentioned in Section 5. Figure 6 shows the posterior distributions of free parameters in the baseline retrieval with the disequilibrium chemistry model. In Table 4, we list the Bayesian evidence of various retrieval models and their comparisons to the baseline model. The CCFs of molecular nondetections are shown in Figure 7. We carry out independent retrievals on two epochs of KIPC data and find broadly consistent posterior constraints as shown in Figure 8. We also explore the effect of correlated noise on the retrieval results by implementing GPs. The corner plot of the posteriors is shown in Figure 9.

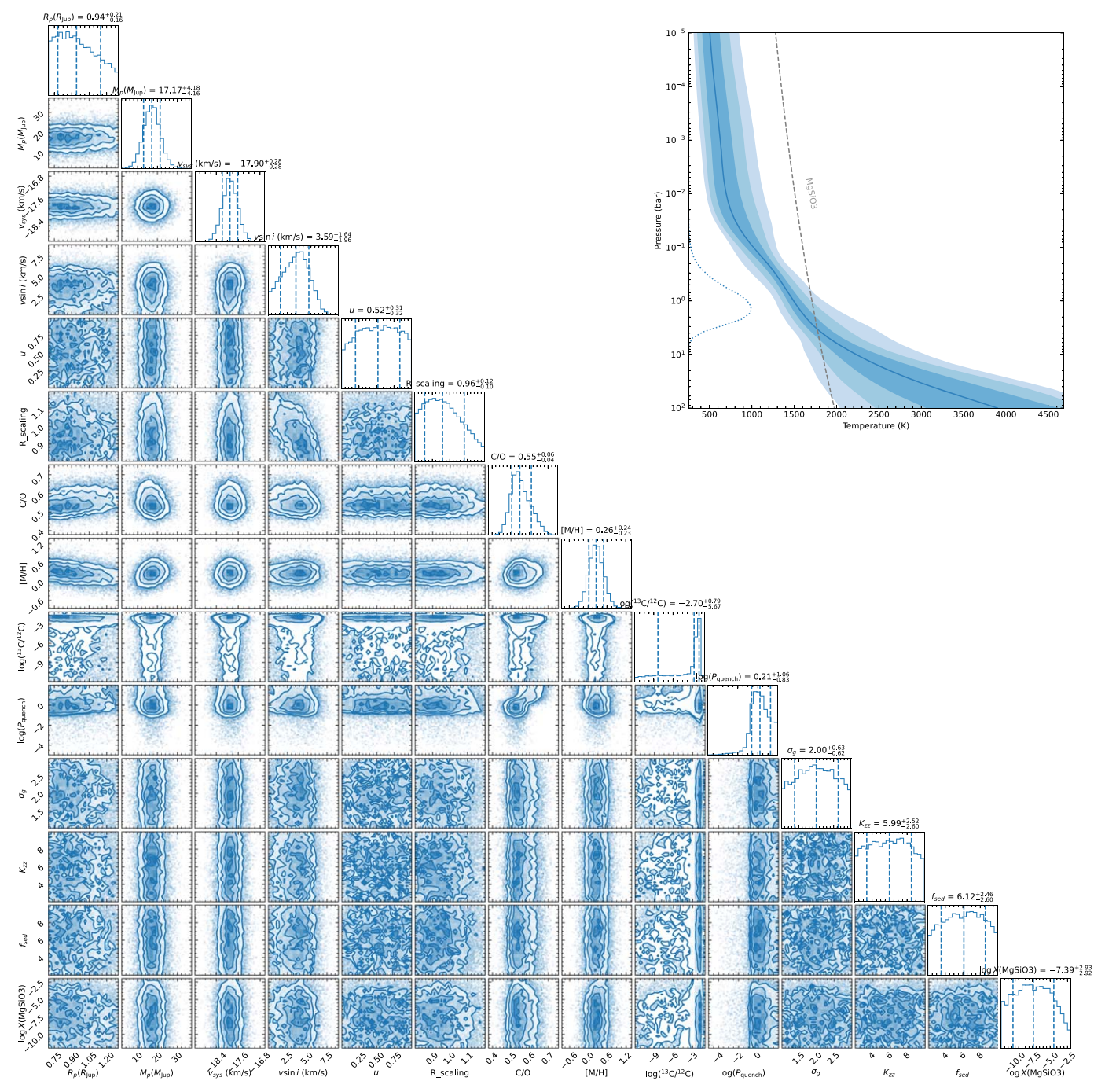


Figure 6. Retrieved posterior distributions of free parameters and the T-P profile in the disequilibrium chemistry model using KPIC observations of HIP 99770 b.

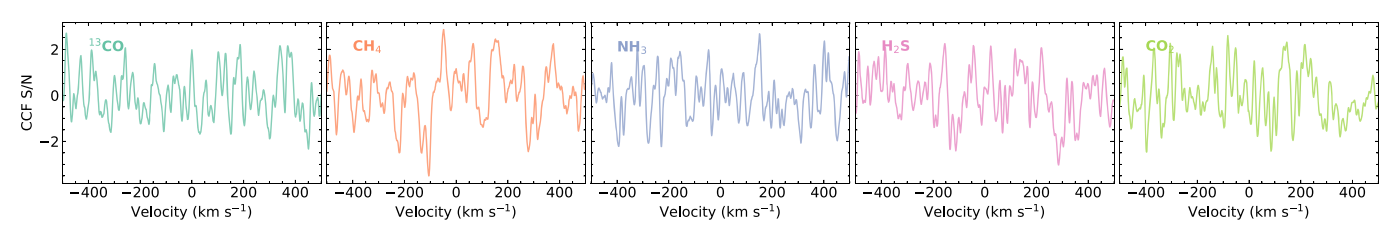


Figure 7. CCFs of nondetected molecules, including ¹³CO, CH₄, NH₃, H₂S, and CO₂.

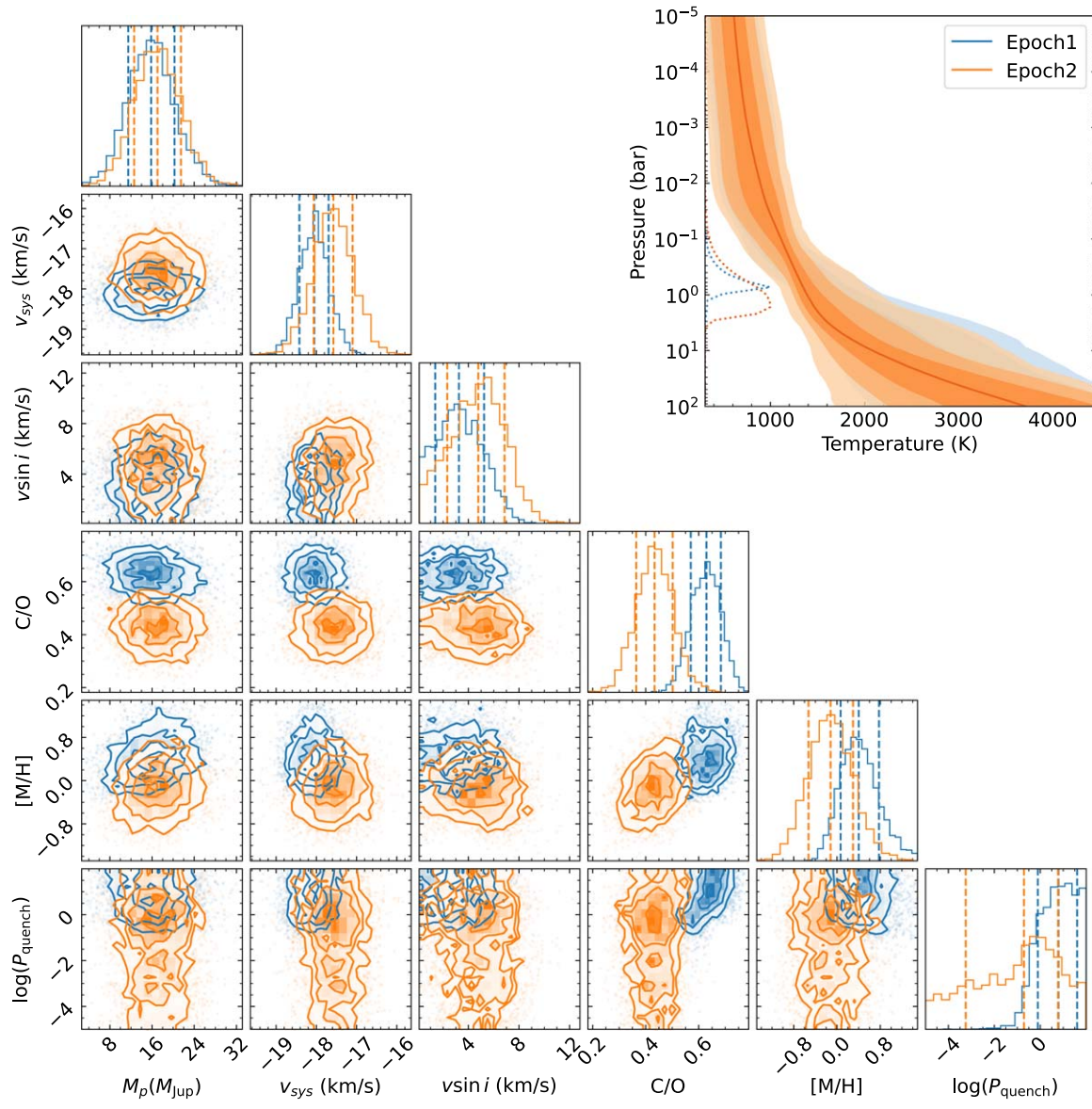


Figure 8. Comparison of independent retrieval analyses on two epochs of observations. The results are consistent within $1\sigma-2\sigma$.

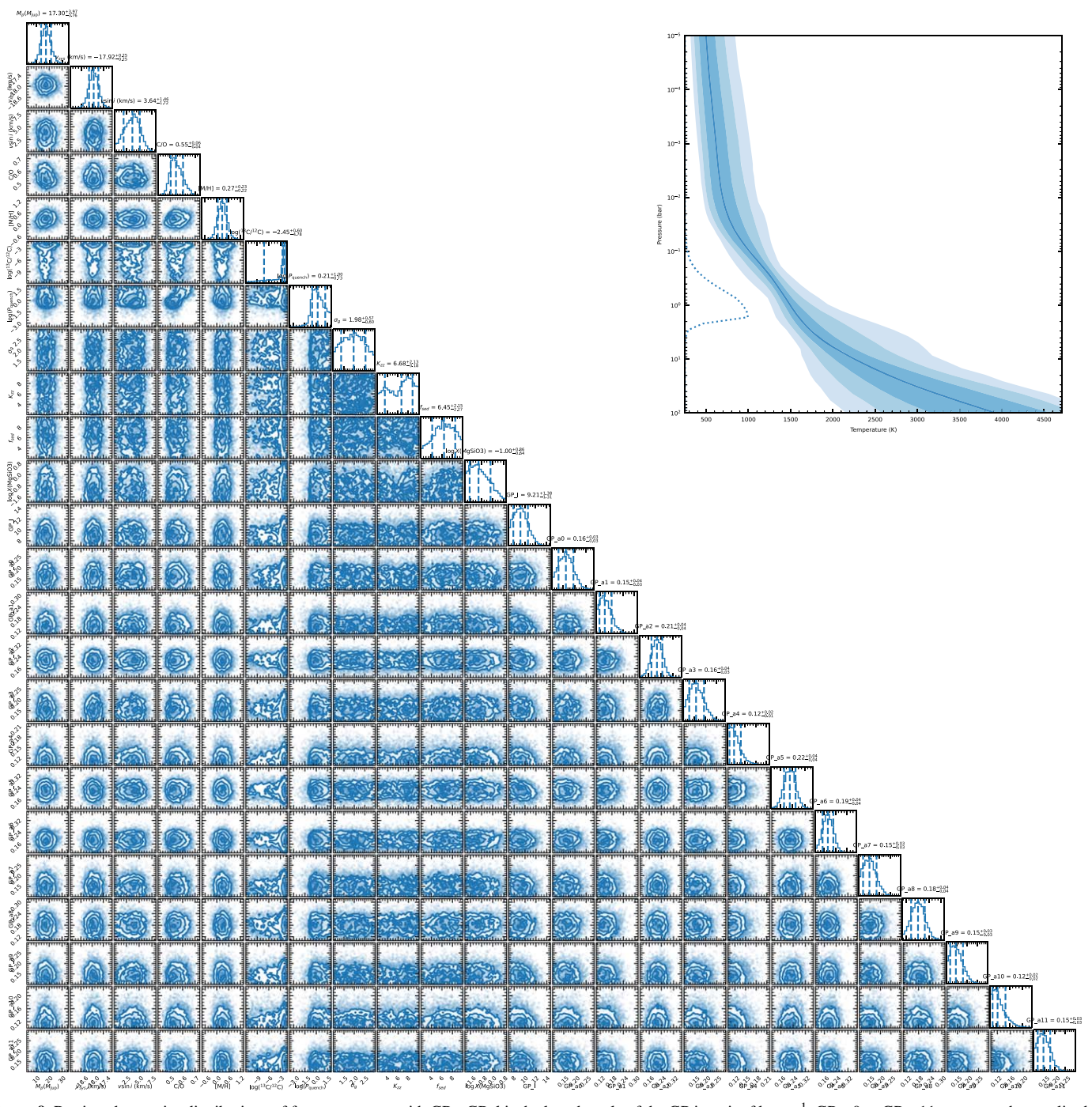


Figure 9. Retrieved posterior distributions of free parameters with GPs. GP_l is the length scale of the GP in unit of km s⁻¹; GP_a0 to GP_a11 represent the amplitude of the GP (in units of typical data uncertainties) for each order in each fiber and epoch. The constraints are fully consistent with the model without GPs.

ORCID iDs

Yapeng Zhang https://orcid.org/0000-0003-0097-4414

Jerry W. Xuan https://orcid.org/0000-0002-6618-1137

Dimitri Mawet https://orcid.org/0000-0002-8895-4735

Jason J. Wang https://orcid.org/0000-0003-0774-6502

Chih-Chun Hsu https://orcid.org/0000-0002-5370-7494

Jean-Bapiste Ruffio https://orcid.org/0000-0003-2233-4821

Heather A. Knutson https://orcid.org/0000-0002-5375-4725

Julie Inglis https://orcid.org/0000-0001-9164-7966

Geoffrey A. Blake https://orcid.org/0000-0003-0787-1610

Yayaati Chachan https://orcid.org/0000-0003-1728-8269

Katelyn Horstman https://orcid.org/0000-0001-9708-8667

Benjamin Calvin https://orcid.org/0000-0003-4737-5486 Jacques-Robert Delorme https://orcid.org/0000-0001-8953-1008

Daniel Echeverri https://orcid.org/0000-0002-1583-2040 Luke Finnerty https://orcid.org/0000-0002-1392-0768 Michael P. Fitzgerald https://orcid.org/0000-0002-0176-8973

Nemanja Jovanovic https://orcid.org/0000-0001-5213-6207 Joshua Liberman https://orcid.org/0000-0002-4934-3042 Ronald A. López https://orcid.org/0000-0002-2019-4995 Evan Morris https://orcid.org/0000-0003-3165-0922 Ben Sappey https://orcid.org/0000-0003-1399-3593

Andrew Skemer https://orcid.org/0000-0001-6098-3924

J. Kent Wallace https://orcid.org/0000-0001-5299-6899

Ji Wang https://orcid.org/0000-0002-4361-8885

Clarissa R. Do O https://orcid.org/0000-0001-5173-2947

References

```
Ackerman, A. S., & Marley, M. S. 2001, ApJ, 556, 872
Agrawal, S., Ruffio, J.-B., Konopacky, Q. M., et al. 2023, AJ, 166, 15
Asplund, M., Amarsi, A. M., & Grevesse, N. 2021, A&A, 653, A141
Astropy Collaboration, Price-Whelan, A. M., Sipőcz, B. M., et al. 2018, AJ,
  156, 123
Baraffe, I., Chabrier, G., Barman, T. S., Allard, F., & Hauschildt, P. H. 2003,
   A&A, 402, 701
Barman, T. S., Konopacky, Q. M., Macintosh, B., & Marois, C. 2015, ApJ,
Batygin, K. 2018, AJ, 155, 178
Benneke, B., & Seager, S. 2013, ApJ, 778, 153
Bitsch, B., Izidoro, A., Johansen, A., et al. 2019, A&A, 623, A88
Bitsch, B., Lambrechts, M., & Johansen, A. 2015, A&A, 582, A112
Bosman, A. D., Alarcón, F., Bergin, E. A., et al. 2021, ApJS, 257, 7
Boss, A. P. 1997, Sci, 276, 1836
Bowler, B. P., Blunt, S. C., & Nielsen, E. L. 2020, AJ, 159, 63
Brandt, T. D. 2021, ApJS, 254, 42
Brandt, T. D., Dupuy, T. J., Li, Y., et al. 2021, AJ, 162, 186
Brown-Sevilla, S. B., Maire, A. L., Mollière, P., et al. 2023, A&A, 673, A98
Bryan, M. L., Benneke, B., Knutson, H. A., Batygin, K., & Bowler, B. P. 2018,
Bryan, M. L., Chiang, E., Bowler, B. P., et al. 2020a, AJ, 159, 181
Bryan, M. L., Ginzburg, S., Chiang, E., et al. 2020b, ApJ, 905, 37
Buchner, J., Georgakakis, A., Nandra, K., et al. 2014, A&A, 564, A125
Burrows, A., Sudarsky, D., & Hubeny, I. 2006, ApJ, 640, 1063
Carvalho, A., & Johns-Krull, C. M. 2023, RNAAS, 7, 91
Chabrier, G. 2003, PASP, 115, 763
Chachan, Y., Knutson, H. A., Lothringer, J., & Blake, G. A. 2023, ApJ,
   943, 112
Coles, P. A., Yurchenko, S. N., & Tennyson, J. 2019, MNRAS, 490, 4638
Currie, T., Brandt, G. M., Brandt, T. D., et al. 2023, Sci, 380, 198
Cushing, M. C., Roellig, T. L., Marley, M. S., et al. 2006, ApJ, 648, 614
de Regt, S., Gandhi, S., Snellen, I., et al. 2024, A&A, 688, A116
Delorme, J.-R., Jovanovic, N., Echeverri, D., et al. 2021, JATIS, 7, 035006
Do Ó, C. R., O'Neil, K. K., Konopacky, Q. M., et al. 2023, AJ, 166, 48
Dürmann, C., & Kley, W. 2015, A&A, 574, A52
Echeverri, D., Jovanovic, N., Delorme, J.-R., et al. 2022, Proc. SPIE, 12184,
   121841W
Erspamer, D., & North, P. 2003, A&A, 398, 1121
Feroz, F., Hobson, M. P., & Bridges, M. 2009, MNRAS, 398, 1601
Finnerty, L., Schofield, T., Delorme, J.-R., et al. 2022, Proc. SPIE, 12184,
Foreman-Mackey, D. 2016, JOSS, 1, 24
Forgan, D., & Rice, K. 2013, MNRAS, 432, 3168
Gaia Collaboration, Brown, A. G. A., Vallenari, A., et al. 2021, A&A, 649, A1 Ginzburg, S., & Chiang, E. 2020, MNRAS, 491, L34
GRAVITY Collaboration, Nowak, M., Lacour, S., et al. 2020, A&A,
   633, A110
Hargreaves, R. J., Gordon, I. E., Rey, M., et al. 2020, ApJS, 247, 55
Harris, C. R., Millman, K. J., van der Walt, S. J., et al. 2020, Natur, 585, 357
Hinkel, N. R., Timmes, F. X., Young, P. A., Pagano, M. D., & Turnbull, M. C.
   2014, AJ, 148, 54
Hoch, K. K. W., Konopacky, Q. M., Theissen, C. A., et al. 2023, AJ, 166, 85
Hoeijmakers, H. J., Schwarz, H., Snellen, I. A. G., et al. 2018, A&A,
   617, A144
Hsu, C.-C., Burgasser, A. J., Theissen, C. A., et al. 2021, ApJS, 257, 45
Hunter, J. D. 2007, CSE, 9, 90
Husser, T. O., Wende-von Berg, S., Dreizler, S., et al. 2013, A&A, 553, A6
Inglis, J., Wallack, N. L., Xuan, J. W., et al. 2024, AJ, 167, 218
Kempton, E. M. R., & Knutson, H. A. 2024, RvMG, 90, 411
```

```
Konopacky, Q. M., Barman, T. S., Macintosh, B. A., & Marois, C. 2013, Sci,
  339, 1398
Kotani, T., Kawahara, H., Ishizuka, M., et al. 2020, Proc. SPIE, 11448,
  1144878
Kratter, K., & Lodato, G. 2016, ARA&A, 54, 271
Lambrechts, M., & Johansen, A. 2012, A&A, 544, A32
Landman, R., Stolker, T., Snellen, I. A. G., et al. 2024, A&A, 682, A48
Le Gal, R., Öberg, K. I., Teague, R., et al. 2021, ApJS, 257, 12
Li, G., Gordon, I. E., Rothman, L. S., et al. 2015, ApJS, 216, 15
Lothringer, J. D., Rustamkulov, Z., Sing, D. K., et al. 2021, ApJ, 914, 12
Madhusudhan, N. 2012, ApJ, 758, 36
Madhusudhan, N., Amin, M. A., & Kennedy, G. M. 2014, ApJ, 794, L12
Marley, M. S., Saumon, D., Visscher, C., et al. 2021, ApJ, 920, 85
Martin, E. C., Fitzgerald, M. P., McLean, I. S., et al. 2018, Proc. SPIE, 10702,
Mawet, D., Ruane, G., Xuan, W., et al. 2017, ApJ, 838, 92
McLean, I. S., Becklin, E. E., Bendiksen, O., et al. 1998, Proc. SPIE, 3354, 566
Mollière, P., Molyarova, T., Bitsch, B., et al. 2022, ApJ, 934, 74
Mollière, P., Stolker, T., Lacour, S., et al. 2020, A&A, 640, A131
Mollière, P., van Boekel, R., Bouwman, J., et al. 2017, A&A, 600, A10
Mollière, P., Wardenier, J. P., van Boekel, R., et al. 2019, A&A, 627, A67
Mordasini, C., van Boekel, R., Mollière, P., Henning, Th., & Benneke, B.
  2016, ApJ, 832, 41
Murphy, S. J., & Paunzen, E. 2017, MNRAS, 466, 546
Nagpal, V., Blunt, S., Bowler, B. P., et al. 2023, AJ, 165, 32
Nasedkin, E., Mollière, P., Lacour, S., et al. 2024, A&A, 687, A298
Nielsen, E. L., De Rosa, R. J., Macintosh, B., et al. 2019, AJ, 158, 13
Öberg, K. I., Guzmán, V. V., Walsh, C., et al. 2021, ApJS, 257, 1
Öberg, K. I., Murray-Clay, R., & Bergin, E. A. 2011, ApJ, 743, L16
Offner, S. S. R., Moe, M., Kratter, K. M., et al. 2023, in ASP Conf. Ser. 534,
  Protostars and Planets VII, ed. S. Inutsuka et al. (San Francisco, CA:
  ASP), 275
Palma-Bifani, P., Chauvin, G., Bonnefoy, M., et al. 2023, A&A, 670, A90
Palma-Bifani, P., Chauvin, G., Borja, D., et al. 2024, A&A, 683, A214
Petrus, S., Whiteford, N., Patapis, P., et al. 2024, ApJL, 966, L11
Pollack, J. B., Hubickyj, O., Bodenheimer, P., et al. 1996, Icar, 124, 62
Polyansky, O. L., Kyuberis, A. A., Zobov, N. F., et al. 2018, MNRAS,
  480, 2597
Qi, C., Öberg, K. I., Andrews, S. M., et al. 2015, ApJ, 813, 128
Robert, C. M. T., Crida, A., Lega, E., Méheut, H., & Morbidelli, A. 2018,
   A&A, 617, A98
Rothman, L. S., Gordon, I. E., Barber, R. J., et al. 2010, JQSRT, 111, 2139
Ruffio, J.-B., Konopacky, Q. M., Barman, T., et al. 2021, AJ, 162, 290
Ruffio, J.-B., Macintosh, B., Konopacky, Q. M., et al. 2019, AJ, 158, 200
Ruffio, J.-B., Perrin, M. D., Hoch, K. K. W., et al. 2023, AJ, 168, 73
Schib, O., Mordasini, C., Wenger, N., Marleau, G. D., & Helled, R. 2021,
    A&A, 645, A43
Schwarz, H., Ginski, C., de Kok, R. J., et al. 2016, A&A, 593, A74
Snellen, I., de Kok, R., Birkby, J. L., et al. 2015, A&A, 576, A59
Spiegel, D. S., & Burrows, A. 2012, ApJ, 745, 174
Turrini, D., Schisano, E., Fonte, S., et al. 2021, ApJ, 909, 40
Veras, D., Crepp, J. R., & Ford, E. B. 2009, ApJ, 696, 1600
Vigan, A., Morsy, M. E., Lopez, M., et al. 2024, A&A, 682, A16
Virtanen, P., Gommers, R., Oliphant, T. E., et al. 2020, NatMe, 17, 261
Vos, J. M., Biller, B. A., Allers, K. N., et al. 2020, AJ, 160, 38
Wang, J., Wang, J. J., Ruffio, J.-B., et al. 2022, AJ, 165, 4
Wang, J. J., Ruffio, J.-B., Morris, E., et al. 2021, AJ, 162, 148
Whiteford, N., Glasse, A., Chubb, K. L., et al. 2023, MNRAS, 525, 1375
Woitke, P., Helling, C., Hunter, G. H., et al. 2018, A&A, 614, A1
Xuan, J. W., Bryan, M. L., Knutson, H. A., et al. 2020, AJ, 159, 97
Xuan, J. W., Hsu, C.-c., Finnerty, L., et al. 2024a, ApJ, 970, 40
Xuan, J. W., Wang, J., Finnerty, L., et al. 2024b, ApJ, 962, 10
Xuan, J. W., Wang, J., Ruffio, J.-B., et al. 2022, ApJ, 937, 54
Zahnle, K. J., & Marley, M. S. 2014, ApJ, 797, 41
Zhang, Y., Snellen, I. A. G., Bohn, A. J., et al. 2021a, Natur, 595, 370
Zhang, Y., Snellen, I. A. G., & Mollière, P. 2021b, A&A, 656, A76
Zhang, Z., Mollière, P., Hawkins, K., et al. 2023, AJ, 166, 198
Zhu, Z., Hartmann, L., Nelson, R. P., & Gammie, C. F. 2012, ApJ, 746, 110
```